Iranian Journal of Materials Forming 13 (1) (2026) 45-58

IJMF

Online ISSN: 2383-0042

Iranian Journal of Materials Forming

Journal Homepage: http://ijmf.shirazu.ac.ir

Research Article

Investigating Hot Deformation Behavior of Ti-6Al-4V Alloy with Fully Lamellar Microstructure Using Work Hardening Rate Characteristic and Processing Map Development

Reza Gostariani * and Gholamreza Vaez

Reactor and Nuclear Safety Research School, Nuclear Science and Technology Research Institute, P.O. Box: 14395-836, Tehran, Iran

ARTICLE INFO

Article history:

Received: 21 September 2025
Reviewed: 2 November 2025
Revised: 3 November 2025
Accepted: 8 November 2025

Keywords:

Hot deformation
Ti-6Al-4V alloy
Work hardening rate
Dynamic recrystallization
Processing map

Please cite this article as:

Gostariani, R., & Vaez, G. (2026). Investigating hot deformation behavior of Ti-6Al-4V alloy with fully lamellar microstructure using work hardening rate characteristic and processing map development. *Iranian Journal of Materials Forming*, *13*(1), 45-58. https://doi.org/10.22099/IJMF.2025.54341.1350

ABSTRACT

In this study, the hot deformation behavior of fully lamellar Ti-6Al-4V alloy was investigated through work hardening rate analysis and processing map development based on experimental hot compression data. Hot compression tests were performed over a temperature range of 700–1050 $^{\circ}$C and strain rates from 0.001 to 1 s^{-1}. Work hardening rate curves were plotted against true stress and true strain using a numerical differentiation method. The results indicated that the work hardening rate increased during straining, reached a maximum, and subsequently decreased to zero due to the activation of dynamic softening mechanisms. The onset of dynamic recrystallization was identified by determining the critical stress from the work hardening rate–stress curve. Dynamic strain aging was detected as fluctuations in the work hardening rate–strain curve. A processing map at a strain of 0.8 was developed to characterize safe and unstable hot deformation domains. Furthermore, microstructural observations were employed to evaluate variations in power dissipation efficiency during hot deformation.

1. Introduction

Ti-6Al-4V alloy is one of the most widely used titanium alloys, revolutionizing industries such as aerospace, energy, defense, medical, and nuclear through its exceptional combination of properties. These include a high strength-to-weight ratio, outstanding fatigue resistance, excellent stability at elevated temperatures, biocompatibility, and superior corrosion resistance [1-3]. However, due to poor workability at ambient temperature caused by the limited number of slip systems in the hexagonal close-packed (HCP) crystal structure of titanium alloys and their sensitivity to

---

[*] Corresponding author
E-mail address: rezagostariani@gmail.com (R. Gostariani)
https://doi.org/10.22099/IJMF.2025.54341.1350

deformation conditions, Ti-6Al-4V alloy is typically formed at elevated temperatures [4, 5]. In addition, grain refinement and the development of favorable mechanical properties are achieved through the hot deformation process. During hot deformation of Ti-6Al-4V, dynamic recrystallization (DRX), dynamic recovery (DRV), and dynamic globularization act as the primary softening mechanisms. These mechanisms play a significant role in influencing the microstructural evolution, thereby improving ductility, strength, and overall mechanical performance [6]. Numerous studies have examined the microstructural evolution of Ti-6Al-4V starting from different initial microstructures, such as equiaxed and lamellar structures. Their findings show that hot deformation of an initial lamellar microstructure within the α phase stability region and at high strain rates tends to produce a kinked microstructure. Conversely, when the strain rate decreases and the temperature increases into the α+β two-phase stability region, the microstructure evolves into a globularized morphology. The kinked microstructure forms through the shearing of α lamellae combined with dynamic recovery, while the globularized microstructure generally develops via dynamic recrystallization [7, 8]. The minimum time required to form a globularized microstructure during inter-pass deformation at a strain of 0.6 has been estimated to be approximately 240 seconds [9].

The critical stress (σ_c) and strain (ε_c) represent fundamental parameters in hot deformation, corresponding to the minimum stress and strain required to initiate dynamic recrystallization (DRX). These parameters are influenced by factors such as chemical composition, deformation conditions, and initial grain size, making their prediction crucial for modeling industrial hot deformation behavior. Although these parameters can be determined through extensive experimental testing and metallographic analysis, this approach presents significant challenges [10]. To overcome these limitations, Ryan and McQueen [11] as well as Poliak and Jonas [12] demonstrated that the critical stress can be identified from the inflection point of the work hardening rate curve plotted against stress ($\theta - \sigma$). Subsequently, Najafizadeh and Jonas [13] further simplified this method by approximating the curve with a third-degree polynomial equation.

Processing maps are essential tools for optimizing the hot deformation of alloys, providing crucial insights into selecting appropriate temperature, strain rate, and strain. Based on the principles of dynamic materials modeling (DMM), processing maps integrate power dissipation efficiency and flow instability criteria to delineate stable and unstable regions during hot working. They identify safe processing windows in which desirable microstructural mechanisms such as dynamic recrystallization and recovery, resulting in improved strength, ductility, and microstructure refinement. In addition, they highlight unstable zones prone to defects such as flow localization, cracking, or void formation. Thus, by utilizing processing maps, it becomes possible to achieve an optimal balance between mechanical properties while minimizing defects and reducing energy consumption in industrial hot deformation processes [14, 15].

To determine the critical stress using the inflection point of the work hardening rate curve plotted against stress ($\theta - \sigma$), one straightforward method is to fit the stress-strain curve ($\sigma - \varepsilon$) using a polynomial equation and then differentiated it with respect to strain to derive the work hardening rate curve. Although this approach effectively mitigates noise from load cell measurements in experimental data, it may reduce the accuracy of critical stress determination. Therefore, in the present work, an alternative method was employed, using numerical differentiation of raw data to construct the work hardening rate curve. The variation of stress with strain was obtained by sequentially calculating numerical differentiation of the hot deformation data over small strain intervals.

In the present study, the hot deformation behavior of Ti-6Al-4V alloy was extensively investigated using work hardening rate curves against true stress and strain, derived via numerical differentiation as a novel method. The initiation of dynamic recrystallization was identified through critical stress calculations based on characteristic changes in the work hardening rate extracted from hot deformation flow curves.

Furthermore, the onset of dynamic strain aging (DSA), which acts as an instability factor during hot deformation, was identified by specific features observed in the work hardening rate-strain curve. Additionally, stable and unstable deformation regions of the Ti-6Al-4V alloy with an initial lamellar microstructure were evaluated using processing maps based on dynamic materials modeling.

2. Materials and Methods

2.1. Specimen preparation and hot compression testing

A cast Ti-6Al-4V ingot produced by vacuum arc remelting (VAR), with its chemical composition detailed in Table 1 and measured precisely using inductively coupled plasma optical emission spectrometry (ICP-OES), was hot forged within the temperature range of 900–1000 °C, followed by air cooling. The ingot was then annealed at 700 °C for 120 minutes and furnace cooled, resulting in a fully lamellar microstructure. The Ti-6Al-4V compression test samples were prepared with a diameter of 9 mm and a height of 13 mm. Isothermal hot compression tests were conducted using a computer-controlled ZwickRoell testing machine with a maximum load capacity of 250 kN, equipped with a radiant cylindrical furnace. The furnace is capable of heating up to 1250 °C and is equipped with a K-type thermocouple regulated by a digital controller, ensuring precise real-time temperature monitoring. This configuration allows the specimen, anvil, and furnace atmosphere (air) to be maintained within ±5 °C throughout all thermomechanical processing stages. Hot compression tests were performed at temperatures ranging from 700 to 1050 °C and strain rates between 0.001 and 1 s^{-1}. Mica sheets were used as a heat-resistant lubricant to minimize friction during testing. After a 10-minutes isothermal heating period at the target deformation temperature, compression was applied until a strain of 0.9 was achieved, after which the sample was rapidly quenched in water. The testing procedure is schematically illustrated in Fig. 1(a). Based on the phase diagram of the alloy shown in Fig. 1(b), the hot compression experiments were conducted across α, α+β, and β phases stability regions [16]. The hot compressive deformation data were corrected for friction effects, adiabatic heating, and strain rate changes during the hot compression test using the method described in Refs [17, 18].

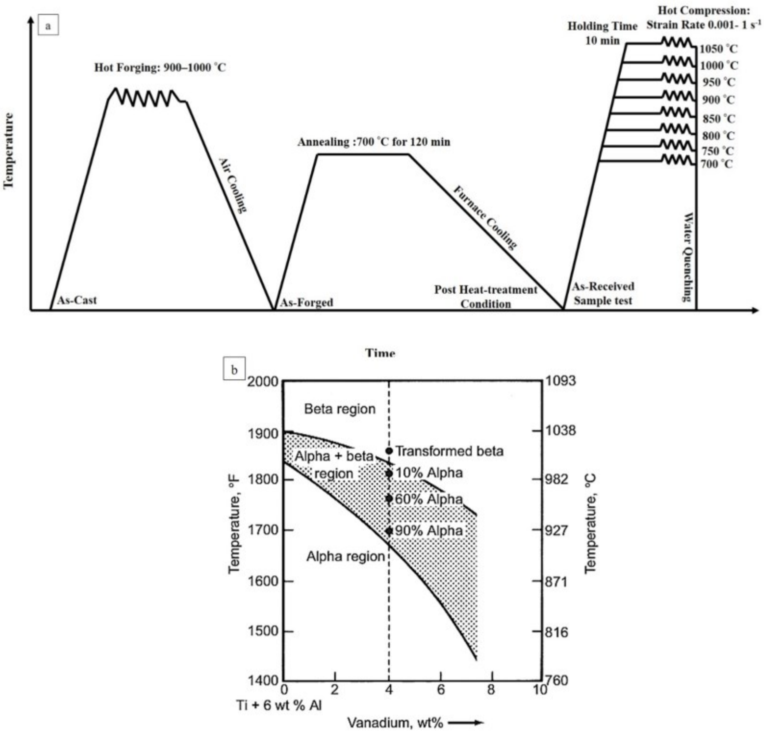

Fig. 1. (a) Schematic illustration of the processing stages of the Ti-6Al-4V sample from forging to the hot compression test, (b) phase stability regions in the Ti-6Al-4V alloy phase diagram [16].

Table 1. Chemical composition of Ti-6Al-4V alloy used in this study

Element	Ti	Al	V	Fe	O	N
Major content (wt. %)	Bal.	6.05	3.99	-	-	-
Impurity content (ppm)	-	-	-	400	400	380

2.2. Critical stress prediction using work hardening rate curve ($d\sigma/d\varepsilon - \sigma$)

The critical stress was determined by identifying the inflection point in the work hardening rate ($d\sigma/d\varepsilon = \theta$) versus stress ($\sigma$) curve. The θ-σ data were derived from experimental hot compression tests conducted at various temperatures and strain rates, as reported in our previous study [6]. In this study, numerical differentiation over small strain intervals was employed to determine the work hardening behavior of the Ti-6Al-4V alloy. The numerical differentiation equation used is presented as:

$$\frac{d\sigma}{d\varepsilon} = \theta = \frac{1}{\varepsilon_{i+n} - \varepsilon_i}\left[(\sigma_{i+n} - \sigma_i) - \frac{1}{2}(\Delta\sigma_{i+n} - \Delta\sigma_i)\right] \quad (1)$$

In this equation, the variable *i* corresponds to the row number in the Excel dataset, and *n* denotes the number of rows used for differentiation. Due to the large dataset, especially at low strain rates, the values of *n* were selected as 80, 30, 2, and 1 for strain rates of 0.001, 0.01, 0.1, and 1 s^{-1}, respectively. For instance, at a strain rate of 0.001 s^{-1}, a spacing of 80 rows between data points was chosen to minimize errors caused by strain data proximity and to smooth the work hardening rate curve. A third-order polynomial ($\theta = A\sigma^3 + B\sigma^2 + C\sigma + D$) was fitted to the obtained work hardening rate data, and the critical stress (σ_c) was subsequently calculated from the inflection point of the fitted curve using the following relationship [13]:

$$\frac{d^2\theta}{d^2\sigma} = 6A\sigma_C + 2B = 0, \rightarrow \sigma_C = (-B)/3A \quad (2)$$

2.3. Processing map based dynamic modeling

The processing map, developed by Prasad using the dynamic materials model, is an effective tool for identifying stable and unstable regions during hot deformation. The analysis is based on the power dissipation coefficient (η), expressed as [14, 15]:

$$\eta = \frac{2\,m}{1 + m} \quad (3)$$

In the improved model designed to reduce error [19], the strain rate sensitivity (*m*) is determined by fitting the $\ln\sigma - \ln\dot{\varepsilon}$ curve using a cubic spline function. This equation is valid when the σ - $\dot{\varepsilon}$ data correspond to a constant temperature and strain. The efficiency map is constructed from a three-dimensional representation of $\eta - T - \dot{\varepsilon}$, which is subsequently visualized in a two-dimensional projection.

The instability map is presented as a 3D plot of $\xi(\dot{\varepsilon})$-T-$\dot{\varepsilon}$. The dimensionless instability parameter of $\xi(\dot{\varepsilon})$ is calculated through two distinct criteria, expressed by the following equations [14, 20]:

$$\xi(\dot{\varepsilon}) = \frac{\partial \ln\left(\frac{m}{1+m}\right)}{\partial \ln\dot{\varepsilon}} + m \leq 0 \quad (4)$$

$$\xi(\dot{\varepsilon}) = 2\,m - \eta < 0 \quad (5)$$

Finally, the processing map at a given strain is constructed by superimposing the instability maps obtained from both criteria onto the power dissipation efficiency map.

2.4. Microstructure evaluation

The microstructural evolution during hot deformation of Ti-6Al-4V was characterized using optical microscopy and scanning electron microscopy (SEM). For analysis, the deformed sample was sectioned longitudinally along the loading axis. The cross-sectioned surface was then ground using sandpaper, polished, and etched with a solution consisting of 85 mL distilled water, 10 mL HNO_3, and 5 mL HF. Fig. 2 illustrates the initial microstructure after heat treatment and prior to hot compression testing. As observed, the microstructure exhibits a well-defined α lamellar morphology with β phase located at the lamellar boundaries.

3. Results and Discussion

3.1. Work hardening characteristic

The corresponding hot compression flow curves were reported in our previous work [6]. Fig. 3 illustrates the

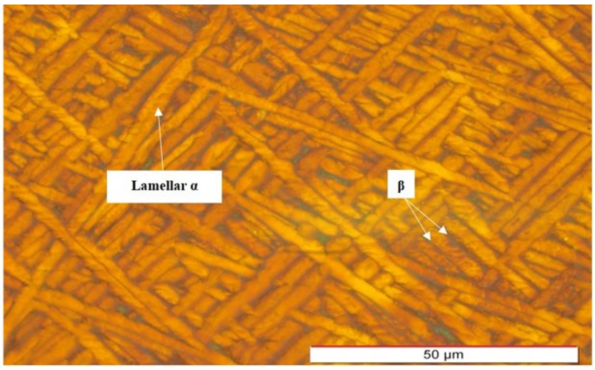

Fig. 2. Initial lamellar microstructure before hot compression.

compressive true stress-strain curve and its work hardening rate-stress curve of Ti-6Al-4V at 950 °C and a strain rate of 1 s^{-1}. As shown in Fig. 3(b), as the stress increases, the work hardening rate increases until it reaches a maximum value. Beyond this peak point, although the work hardening rate remains positive, its slope with respect to stress decreases. The peak stress is determined at the point where the work hardening rate curve intersects the zero. As shown, this peak stress is approximately 39 MPa which is consistent with the true stress-strain curve in Fig. 3(a). The changes observed in the work hardening rate-stress curve are attributed to variations in dislocation density during hot deformation. As shown in Fig. 3(b), this curve can be divided into four stages. The first of which extends from the initial stress to the region where the work hardening rate increases linearly with stress. Then, the increase in work hardening rate becomes nonlinear until reaching its maximum value. In these two stages, the change in stress is accompanied by intense dislocation multiplication. In the third stage, while dislocation generation and work hardening mechanisms dominate, the work hardening rate decreases due to the rearrangement and a reduction in the rate of dislocation accumulation. This behavior is associated with back stress effects and the formation of dislocation cells and sub-grains [21]. The end of stage three corresponds to the onset of dynamic recrystallization and the critical stress. In addition, the decrease in the work hardening rate in the third stage exhibits two different slopes, and the intersection stress of these two slopes is marked with an arrow (21.33 MPa). By comparison with Fig. 3(a), this point appears to correspond to the deviation of the stress-strain curve from linear behavior. Subsequently, in the fourth stage, the slope of deformation changes until the material reaches the peak stress.

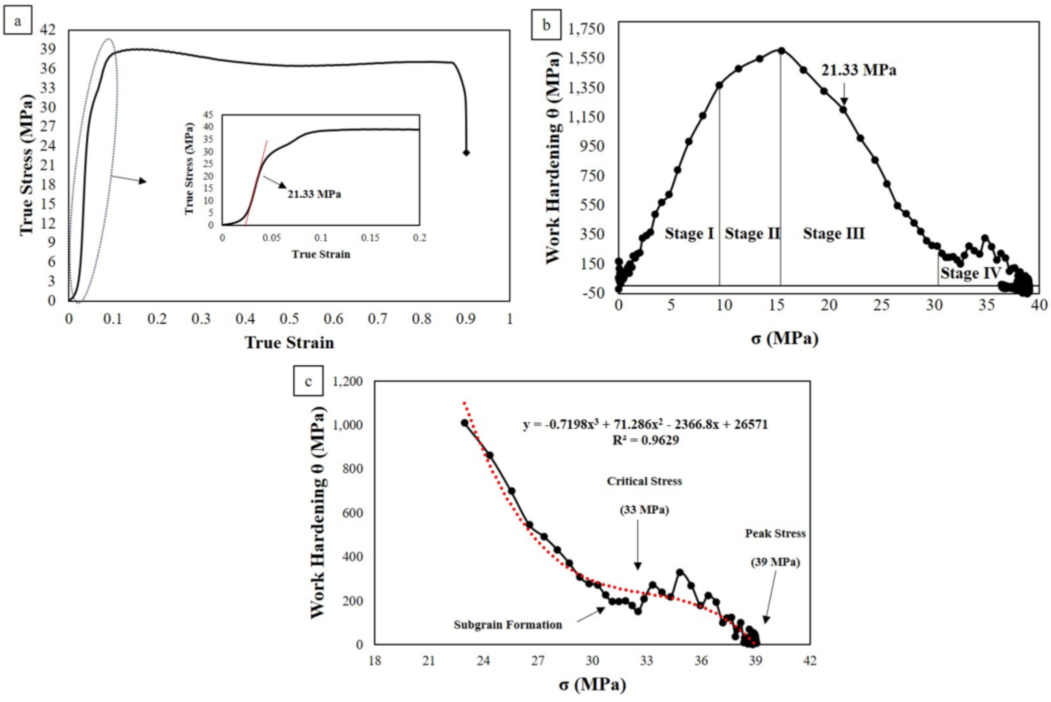

Fig. 3. True stress-strain and work hardening rate curves of Ti-6Al-4V at 950 °C and a strain rate of 1 s^{-1}: (a) true stress-strain curve, (b) complete work hardening rate curve, (c) detailed section of the work hardening rate curve used to identify the critical stress.

The critical point was determined by identifying the inflection point on the $\theta - \sigma$ curve fitted with a third-degree polynomial (Fig. 3(c)). Using the corresponding equation, the critical stress was calculated to be 33 MPa.

Fig. 4 shows the descending portion of the $\theta - \sigma$ curve for different temperatures and strain rates. The constants of the polynomial equation fitted to each curve, along with the corresponding inflection point, indicating the critical stress, are listed in Table 2. It is evident that as temperature increases and strain rate decreases; the critical stress values decrease accordingly. As shown in Fig. 4, dynamic recrystallization (DRX) occurs across all tested temperatures and strain rates, including those within the β phase region. At 1000 ˚C and 1050 ˚C (β phase), the work hardening initially decreases up to a certain point, corresponding to sub-grain formation.

Table 2. Polynomial equation and critical stress of Ti-6Al-4V Alloy at various temperatures and strain rates

Strain rate	**Temperature**	**Polynomial equation** $\theta = A\,\sigma^3 + B\,\sigma^2 + C\,\sigma + D$				**Critical stress**	σ_c/σ_p
		A	**B**	**C**	**D**		
$0.001 s^{-1}$	700 ˚C	-0.0428	26.186	- 5408.3	380261	203.94 MPa	0.87
	750 ˚C	-0.068	26.993	- 3645.4	169833	132.18 MPa	0.85
	800 ˚C	-0.0177	3.2606	- 240.75	8826.3	61.4 MPa	0.63
	850 ˚C	-0.152	20.398	- 916.75	14973	44.73 MPa	0.69
	900 ˚C	0.2578	- 30.666	1013.6	- 7829.4	39.65 MPa	0.96
	950 ˚C	-136.8	3847.1	- 36135	113648	9.37 MPa	0.77
	1000 ˚C	7.2969	- 143.64	841.11	- 1217.3	6.56 MPa	0.74
	1050 ˚C	-5.9533	114.96	-768.19	1822.2	6.43 MPa	0.84
$0.01 s^{-1}$	700 ˚C	-0.0042	2.5377	- 549.67	48249	201.40 MPa	0.70
	750 ˚C	-0.0006	- 0.2662	57.745	3668.7	147.88 MPa	0.74
	800 ˚C	-0.1209	47.833	- 6369.5	287992	131.88 MPa	0.86
	850 ˚C	-0.0669	13.878	- 969.93	24467	69.15 MPa	0.72
	900 ˚C	-0.0149	- 1.9381	138.17	1191.6	43.36 MPa	0.76
	950 ˚C	-2.6791	149.96	- 2924.9	20434	18.65 MPa	0.79
	1000 ˚C	5.1401	- 178.92	1847.7	- 4760.2	11.60 MPa	0.74
	1050 ˚C	4.6926	- 141.31	1264.4	- 2834.1	10.04 MPa	0.76
$0.1 s^{-1}$	700 ˚C	-0.0118	9.6083	- 2622.3	242929	271.42 MPa	0.86
	750 ˚C	-0.0237	16.377	- 3848.3	309798	230.33 MPa	0.87
	800 ˚C	-0.1225	71.542	- 13997	919359	194.67 MPa	0.91
	850 ˚C	-0.1782	62.711	- 7376.8	291415	117.3 MPa	0.86
	900 ˚C	-0.2737	63.145	- 4959.4	134328	76.90 MPa	0.86
	950 ˚C	1.5726	- 124.57	3054.1	- 21748	26.4 MPa	0.84
	1000 ˚C	2.753	- 182.22	3749.8	- 22630	22.06 MPa	0.83
	1050 ˚C	-1.1934	78.302	- 1755.9	13551	21.87	0.90
$1 s^{-1}$	700 ˚C	0.0068	- 5.4102	1329.5	- 94226	265.2 MPa	0.81
	750 ˚C	-0.0142	9.9885	- 2400.6	198322	234.47 MPa	0.91
	800 ˚C	-0.0416	22.453	- 4117.8	260560	179.91 MPa	0.84
	850 ˚C	-0.1275	50.129	- 6618	295446	131.06 MPa	0.86
	900 ˚C	-0.0364	8.2425	- 651.51	18373	75.48 MPa	0.85
	950 ˚C	-0.7198	71.286	- 2366.8	26571	33.01 MPa	0.85
	1000 ˚C	2.1796	- 141.51	2845.4	- 16571	21.64 MPa	0.76
	1050 ˚C	0.4157	- 26.054	477.91	- 2086.1	20.89 MPa	0.76

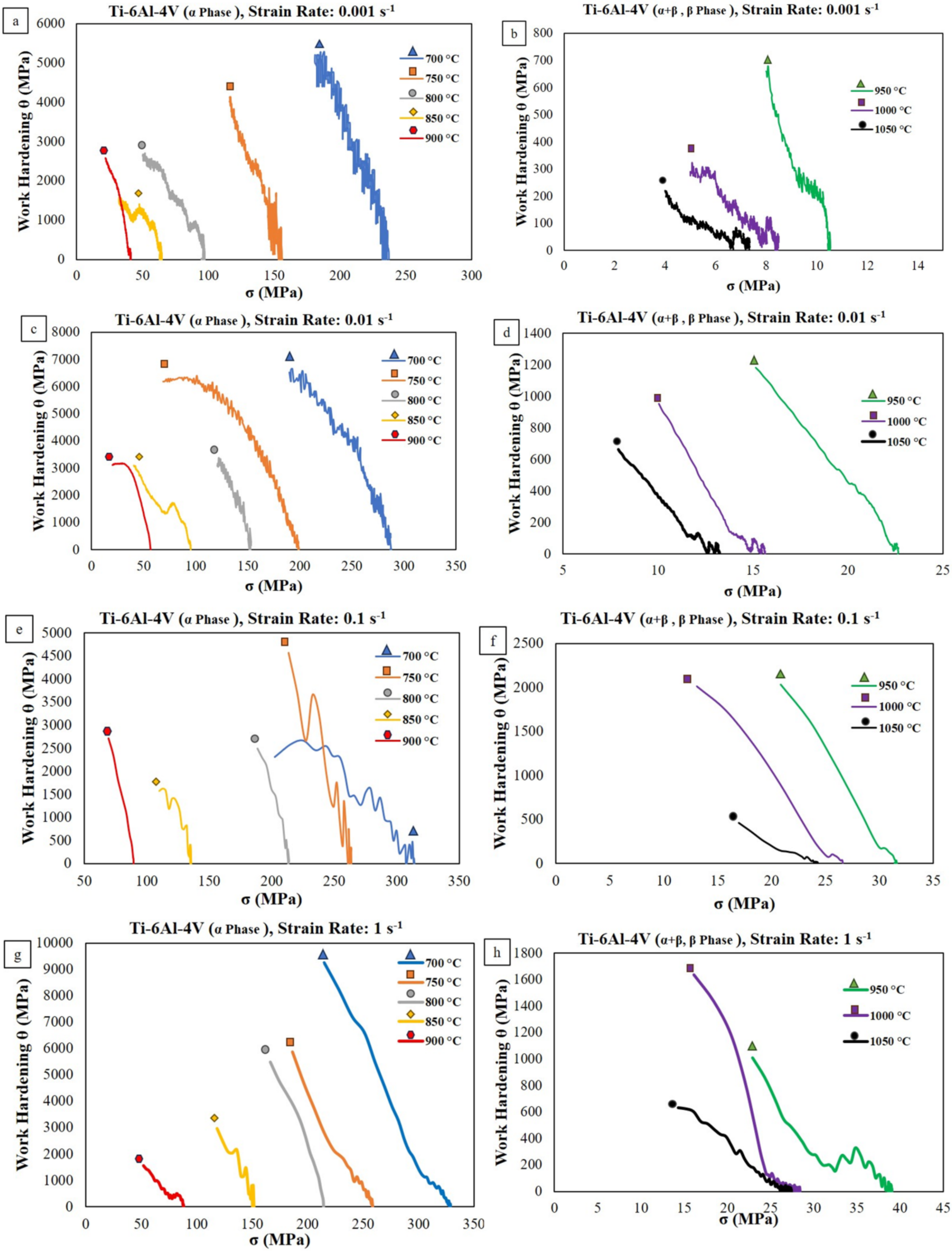

Fig. 4. Work hardening rate versus true stress curves of Ti-6Al-4V alloy at various temperatures ranging from 700 to 1050 °C and strain rates of (a, b) 0.001 s^{-1}, (c, d) 0.01 s^{-1}, (e, f) 0.1 s^{-1}, (g, h) 1 s^{-1}.

Subsequently, with the onset of work hardening in the recrystallized grains, the work hardening rate increases and then decreases again until reaching the peak stress. These results are consistent with the activation energy obtained for the β phase in our previous study [6], which was approximately 291 kJ/mol, significantly higher than the self-diffusion activation energy value of 97-153 kJ/mol reported in the literature [22, 23].

Fig. 5 illustrates the relationship between the peak experimental stress and the critical stress calculated using the polynomial equation. As shown, these parameters are closely related, with $\sigma_c/\sigma_p \cong 0.827$.

The critical strain (ε_c) initiating dynamic recrystallization and dynamic strain aging (DSA) behavior of Ti-6Al-4V alloy are determined from the work hardening rate – true strain (θ-ε) curves. Dynamic strain aging is a phenomenon arising from the interaction of impurity elements with dislocation cores, manifested as Lüders bands and the Portevin–Le Chatelier effect in the hot stress-strain deformation curve [24, 25]. Fig. 6 shows the θ-ε curves at temperatures and strain rates of 700 ˚C-0.01 s^{-1}, 950 ˚C-1 s^{-1}, 850 ˚C-1 s^{-1}, and 800 ˚C-1 s^{-1}. Based on Fig. 6(b), the curve can be divided into three stages. In stage I, the work hardening rate increases linearly. Stage II marks the onset of dynamic strain aging, with fluctuations associated with dislocation movement. In stage III, the work hardening rate decreases until reaching the peak strain. The critical strain is estimated from the deviation in slope observed during stage III, as shown in Fig. 6(d).

As shown in Fig. 6, dynamic strain aging fluctuations are clearly observed in the work hardening rate curves. Experimental results generally indicate that with increasing temperature, strain, and strain rate, the intensity of DSA tends to decrease. This behavior is attributed to enhanced dislocation mobility and facilitated dislocation climb at higher temperatures, while higher strain rates reduce the diffusion rate of impurity atoms. However, as noted in other study [26], DSA occurs within a specific temperature range. Despite the increased dislocation mobility at elevated temperatures, both the diffusion rate of impurities and dislocation pinning effects also increase. As illustrated in Fig. 6(e), the intensity of DSA reaches a maximum at 850 ˚C and a strain rate of 1 s^{-1}, while it diminishes at temperatures above and below this point, as shown in Figs. 6(c) and 6(f).

3.2. Processing map

Fig. 7 shows the power efficiency map of the Ti-6Al-4V alloy at a strain of 0.8. As can be seen, the efficiency varies from negative values (blue region) to about 55 % (red region). The region with negative efficiency is recognized as unstable domain in hot deformation. In contrast, the softening mechanism during hot deformation such as dynamic recovery, dynamic recrystallization, and super-plasticity occur within efficiency ranges of approximately 10-30 %, 35-55 % [27, 28], and > 60 % [28], respectively. According to the power efficiency map, hot deformation in the temperature range of 800 to 950 ˚C and strain rates between 0.001 s^{-1} and 0.01 s^{-1} exhibits the highest power efficiency.

Fig. 8(a, b) shows the instability maps based on the two criteria described in section 2.3. Fig. 8(a) corresponds to the blue region in Fig. 7. Hot deformed instabilities occur in the temperature ranges of 750-775 ˚C and 1000-1025 ˚C at high strain rates of 0.6-1 s^{-1}. The primary instability in the α phase region at 750-775 ˚C and a strain rate of 1 s^{-1} involves sharp cracking and adiabatic shear band formation [29, 30]. This instability arises from increased strain rates causing localized adiabatic heating, which raises the sample temperature

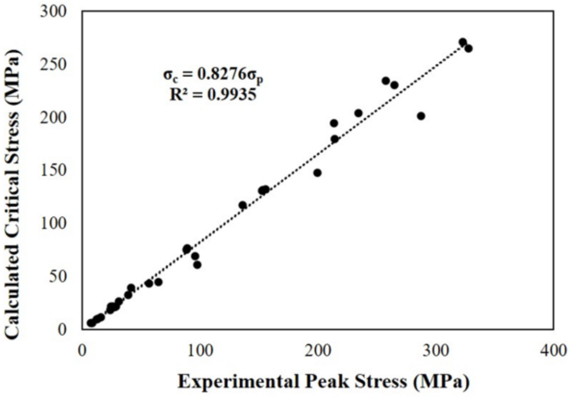

Fig. 5. Relationship between experimental peak stress and critical stress in Ti-6Al-4V alloy.

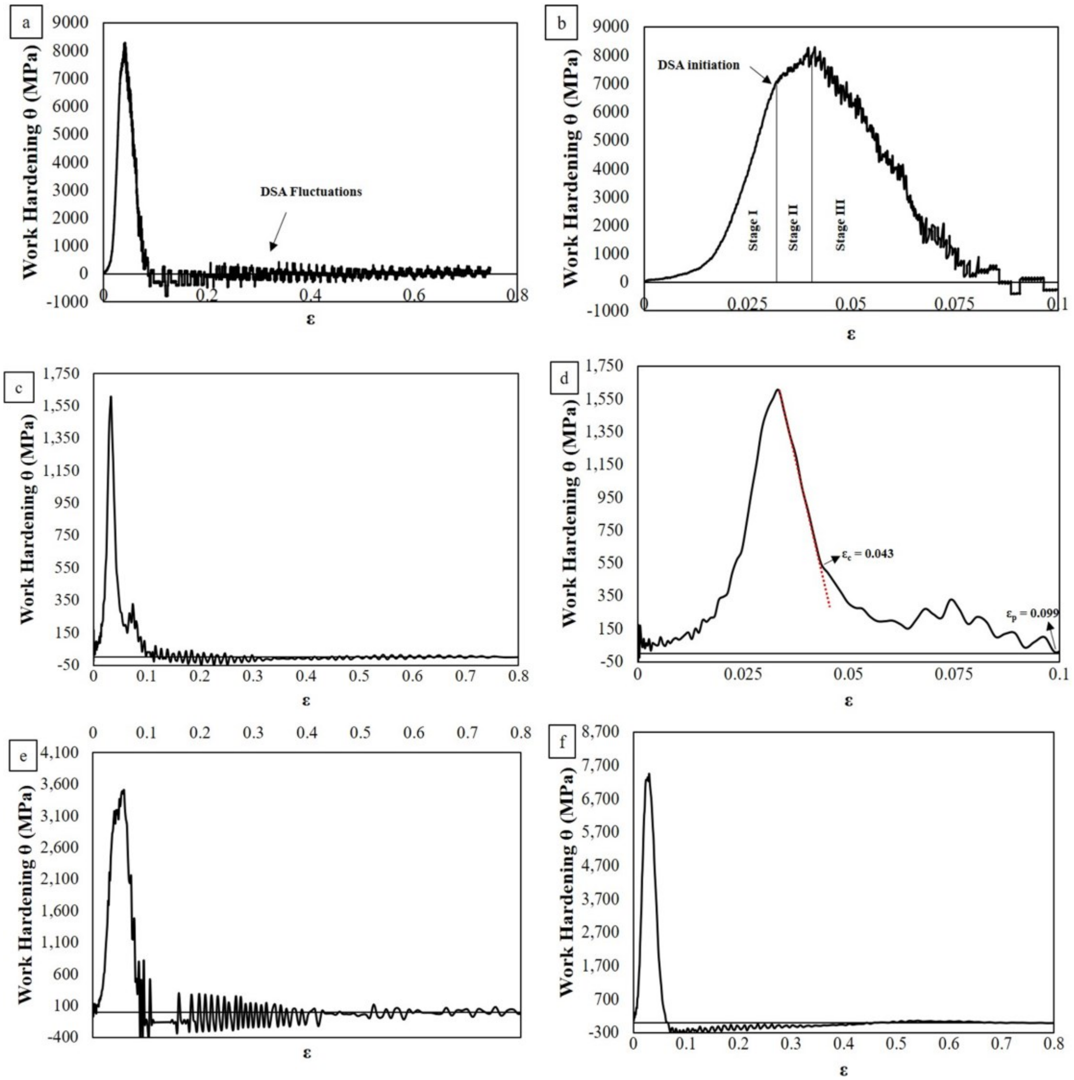

Fig. 6. Work hardening rate versus strain curves of Ti-6Al-4V alloy at (a, b) 700 ˚C and 0.01 s⁻¹, (c, d) 950 ˚C and 1 s⁻¹, (e) 850 ˚C and 1 s⁻¹, and (f) 800 ˚C and 1 s⁻¹.

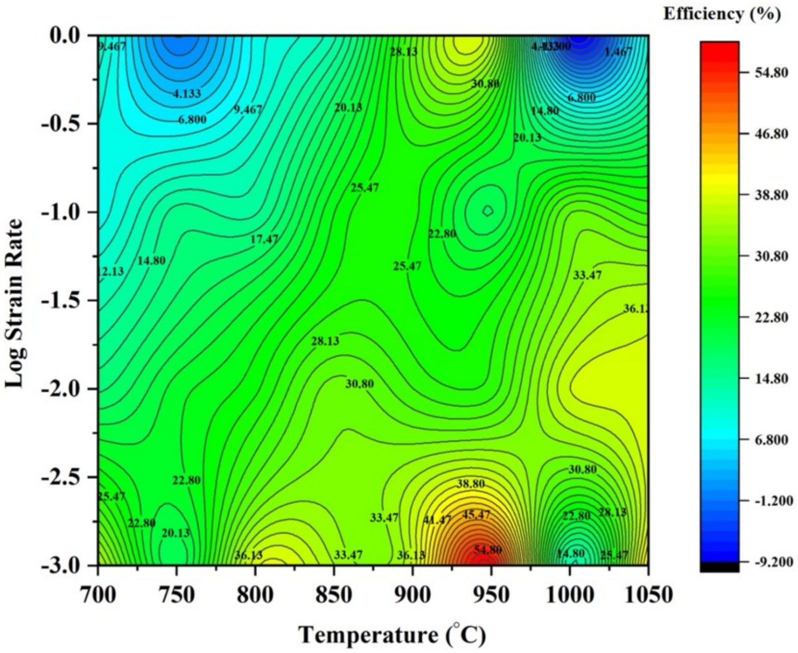

Fig. 7. The power efficiency map of the Ti-6Al-4V alloy in strain of 0.8.

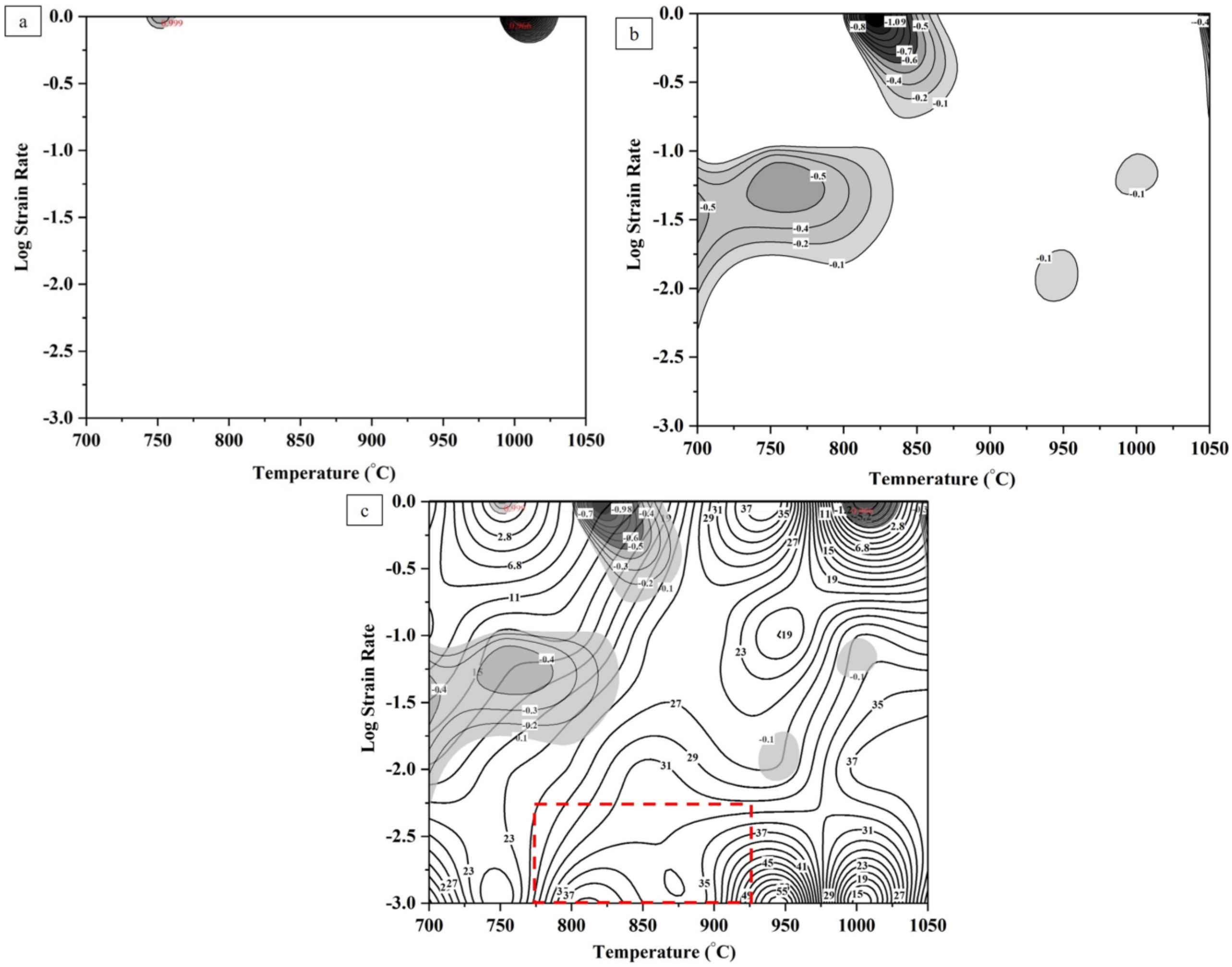

Fig. 8. (a) The instability map with criteria of $\xi(\dot{\varepsilon}) = 2m - \eta < 0$, (b) the instability map with criteria of $\xi(\dot{\varepsilon}) = \frac{\partial \ln(\frac{m}{1+m})}{\partial \ln \dot{\varepsilon}} + m \leq 0$, (c) processing map of Ti-6Al-4V alloy.

and suppresses microstructural evolution due to insufficient thermal exposure. Conversely, instability in the β-phase appears at 1000-1050 ˚C and a strain rate of 1 s^{-1}. The second instability regions are observed in the temperature and strain rate ranges of 700-825 ˚C, 0.01-0.1 s^{-1} and 800-875 ˚C, 0.1-1 s^{-1}. Lamellar kinking is responsible for this instability at intermediate strain rates [29]**.** The processing map constructed by superimposing the efficiency and instability maps is illustrated in Fig. 8(c). The processing window, highlighted by the red square frame in Fig. 8(c) delineates the safe region for Ti-6Al-4V alloy, corresponding to a temperature range of 775–925 ˚C and strain rate ranges of 0.001–0.005 s^{-1}. This region provides not only high-power dissipation efficiency but is located far from the instability zones.

3.3. Microstructure observations

Microstructural evolution generally aligns with processing maps and is used to validate them. The hot-deformed microstructures are shown in Fig. 9. As seen previously in Fig. 2, the as-received microstructure is lamellar, consisting of fully lamellar α layers with β phase at the boundaries. The hot deformed microstructures evolve through dynamic recovery, dynamic recrystallization and globularization. The breakdown of the lamellar microstructure and its transformation into a globular microstructure is considered a desirable microstructural objective in the thermo-mechanical processing of Ti-6Al-4V alloy. This process, occurring below the β phase transformation temperature, improves fatigue crack growth resistance and fracture toughness [7]. Based on processing map, the hot deformed microstructures of Ti-6Al-4V alloy in low power efficiency condition at 700 °C-0.1 s^{-1}, 750 °C-1 s^{-1} and 850 °C-1 s^{-1} are presented in Fig. 9(a- c). The lamellar α becomes kinked under compressive stress, the thickness decreases, and shear bending causes fragmentation of the α layer, leading to the formation of broken lamellar islands. The microstructures in Figs. 9(a) and 9(b) fall within the instability region of the processing map. Since microcracks and flow localization are not clearly visible in the optical micrograph [28], direct evidence of these defects is not observed. However, inhomogeneity in hot deformation, as an indicator of microstructural instability [28], is apparent in these microstructures.

With increasing power efficiency, achieved by raising the temperature and reducing the strain rate, the dynamic recrystallization and globularization mechanisms promote the formation of equiaxed microstructures. Figs. 9(d-f) show the microstructures after deformation at 900 °C with strain rates of 0.001 s^{-1} and 0.01 s^{-1}, corresponding to conditions within the processing window. As observed, at this temperature and a power efficiency level of 35%, the microstructure undergoes significant globularization.

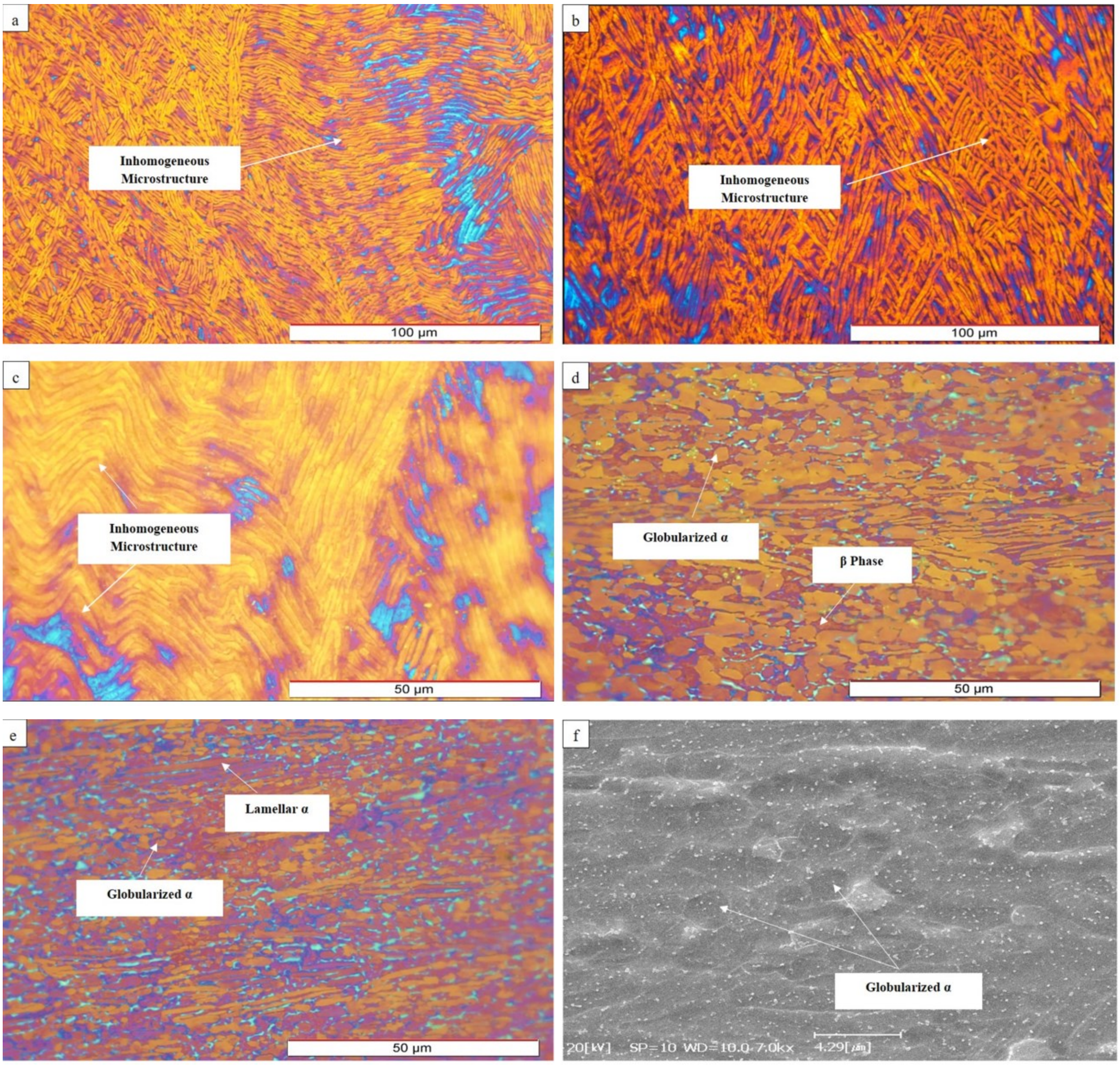

Fig. 9. Hot-deformed microstructure of the Ti-6Al-4V alloy at different temperatures and strain rates, corresponding to stable and unstable regions of the processing map. (a) 700 °C-0.1 s^{-1}, (b) 750 °C-1 s^{-1}, (c) 850 °C-1 s^{-1}, (d) 900 °C-0.001 s^{-1}, (e) 900 °C-0.01 s^{-1}, (f) SEM micrograph of 900 °C-0.01 s^{-1}.

However, portions of the microstructure remain lamellar, and the fraction of the lamellar microstructure increases as the strain rate increases from 0.001 s^{-1} to 0.01 s^{-1}. During globularization, the thickness of α layers were decreased due to increased strain localization. Diffusion of the β phase in α layer accelerates and appears as grooves within the lamellar. This phenomenon led to α layer fragmentation and the microstructure converted to equiaxed morphology [6, 31, 32].

4. Conclusions

This study comprehensively examined the hot deformation behavior of Ti-6Al-4V alloy through detailed analyses of work hardening characteristics, critical stress and strain determinations, dynamic strain aging phenomena, processing maps, and microstructural evolution. Hot compression tests were conducted over a temperature range of 700-1050 ˚C and strain rates of 0.001-1 s^{-1}. Numerical differentiation combined with third-degree polynomial fitting provided a precise method for identifying the critical stress and strain corresponding to the onset of dynamic recrystallization (DRX). The principal findings of this study can be summarized as follows:

- The ratio of calculated critical stress to experimental peak stress was accurately estimated at approximately 0.82.
- Critical strain values derived from work hardening rate–strain curves revealed oscillatory features signifying the onset and progression of dynamic strain aging (DSA).
- DSA effects diminished with increasing temperature, strain, and strain rate, but intensified within a specific temperature range governed by impurity-particle-diffusion-related softening mechanisms.
- Processing maps revealed stable deformation windows, notably between 775 and 925 ˚C at strain rates of 0.001–0.005 s^{-1}, characterized by high power dissipation efficiency and minimal flow instability.
- Microstructural observations confirmed the transformation from lamellar to globular α phases via dynamic recovery, DRX, and globularization mechanisms. At higher strain rates, flow instability manifested as microstructural heterogeneity within the alloy.

Authors' contributions

R. Gostariani: Conceptualization, Validation, Formal analysis, Investigation, Writing – original draft, Review & editing

G. Vaez: Methodology, Data curation

Conflict of interest

The authors declare that there is no conflict of interest regarding the publication of this paper.

Funding

The research was supported by Atomic Energy Organization of Iran.

5. References

[1] Ji, S. M., Jang, S. M., Lee, Y. S., Kwak, H. M., Choi, J. M., & Joun, M. S. (2022). Characterization of Ti-6Al-4V alloy in the temperature range of warm metal forming and fracture analysis of the warm capping process. *Journal of Materials Research and Technology, 18*, 1590-1606. https://doi.org/10.1016/j.jmrt.2022.03.066

[2] Pilehva, F., Zarei-Hanzaki, A., Fatemi-Varzaneh, S., & Khalesian, A. (2015). Hot deformation and dynamic recrystallization of Ti-6Al-7Nb biomedical alloy in single-phase β region. *Journal of Materials Engineering and Performance*, 24(5), 1799-1808. https://doi.org/10.1007/s11665-015-1468-3

[3] Leyens, C., & Peters, M. (2006). *Titanium and titanium alloys: fundamentals and applications*, Wiley Online Library.

[4] Chen, G., Ren, C., Qin, X., & Li, J. (2015). Temperature dependent work hardening in Ti–6Al–4V alloy over large temperature and strain rate ranges: Experiments and constitutive modeling, *Materials & Design.* 83, 598-610. https://doi.org/10.1016/j.matdes.2015.06.048

[5] Jiang, F., Fei, L., Jiang, H., Zhang, Y., Feng, Z., & Zhao, S. (2023). Constitutive model research on the hot deformation behavior of Ti6Al4V alloy under wide temperatures. *Journal of Materials Research and Technology*, *23*, 1062-1074. https://doi.org/10.1016/j.jmrt.2023.01.021

[6] Gostariani, R., Vaez, G., Ansaripour, M., & Babanejad, A. (2024). Constitutive modeling and microstructural evolution of hot deformed Ti-6Al-4V alloy starting with

initial fully lamellar microstructure. *Iranian Journal of Materials Forming, 11*(2), 30-45. https://doi.org/10.22099/ijmf.2024.49974.1292

[7] Jha, J. S., Toppo, S. P., Singh, R., Tewari, A., & Mishra, S. K. (2019). Flow stress constitutive relationship between lamellar and equiaxed microstructure during hot deformation of Ti-6Al-4V. *Journal of Materials Processing Technology*, *270*, 216-227. https://doi.org/10.1016/j.jmatprotec.2019.02.030

[8] Lin, Y. C., Wu, Q., Pang, G. D., Jiang, X. Y., & He, D. G. (2020). Hot tensile deformation mechanism and dynamic softening behavior of Ti–6Al–4V alloy with thick lamellar microstructures. *Advanced Engineering Materials*, *22*(3), 1901193. https://doi.org/10.1002/adem.201901193

[9] Ezatpour, H., Ebrahimi, G., & Zarghani, F., (2024). Effect of processing parameters on the morphology of α-phase in Ti-6Al-4V alloy during the two-step hot deformation. *Iranian Journal of Materials Forming*, *10*(3), 54-62. https://doi.org/10.22099/ijmf.2024.49049.1277

[10] Mirzadeh, H., & Najafizadeh, A. (2010). Prediction of the critical conditions for initiation of dynamic recrystallization. *Materials & Design, 31*(3), 1174-1179. https://doi.org/10.1016/j.matdes.2009.09.038

[11] Ryan, N., & McQueen, H. (1990). Dynamic softening mechanisms in 304 austenitic stainless steel. *Canadian Metallurgical Quarterly*, *29*(2), 147-162. https://doi.org/10.1179/cmq.1990.29.2.147

[12] Poliak, E. I., & Jonas, J. J. (2003). Initiation of dynamic recrystallization in constant strain rate hot deformation. *ISIJ International, 43*(5), 684-691. https://doi.org/10.2355/isijinternational.43.684

[13] Najafizadeh, A., & Jonas, J. J. (2006). Predicting the critical stress for initiation of dynamic recrystallization. *ISIJ International, 46*(11), 1679-1684. https://doi.org/10.2355/isijinternational.46.1679

[14] Prasad, Y. (2003). Processing maps: A status report, *Journal of Materials Engineering and Performance*. *12*(6), 638-645. https://doi.org/10.1361/105994903322692420

[15] Prasad, Y. V. R. K., Gegel, H. L., Doraivelu, S. M., Malas, J. C., Morgan, J. T., Lark, K. A., & Barker, D. R. (1984). Modeling of dynamic material behavior in hot deformation: Forging of Ti-6242. *Metallurgical Transactions A*, *15*(10), 1883-1892. https://doi.org/10.1007/BF02664902

[16] Donachie, M. J. (2000). *Titanium: a technical guide*. ASM International.

[17] Gostariani, R., & Asadi Asadabad, M. (2023). Studying the hot deformation behavior of Zr-1Nb alloy using processing map and kinetic analysis. *Journal of Materials Engineering and Performance*, *32*(5), 2151-2164. https://doi.org/10.1007/s11665-022-07267-5

[18] Gostariani, R., Ebrahimi, R., & Asadi Asadabad, M. (2018). The study of hot deformation behavior of mechanically milled and hot extruded Al–BN nanocomposite. *Transactions of the Indian Institute of Metals, 71*(5), 1127-1136. https://doi.org/10.1007/s12666-017-1248-x

[19] Eskandari, H., Reihanian, M., & Alavi Zaree, S. (2023). An analysis of efficiency parameter and its modifications utilized for development of processing maps. *Iranian Journal of Materials Forming*, *10*(4), 45-51. https://doi.org/10.22099/ijmf.2024.49537.1283

[20] Ebrahimi, R., Najafizadeh, A. (2004). Optimization of hot workability in ti-if steel by using the processing map. *International Journal of ISSI*, *1*(1), 1-7.

[21] Kumar, S. S., Raghu, T., Bhattacharjee, P. P., Rao, G. A., & Borah, U. (2017). Work hardening characteristics and microstructural evolution during hot deformation of a nickel superalloy at moderate strain rates. *Journal of Alloys and Compounds, 709*, 394-409. https://doi.org/10.1016/j.jallcom.2017.03.158

[22] Ning, Y., Xie, B., Liang, H., Li, H., Yang, X., Guo, H. (2015). Dynamic softening behavior of TC18 titanium alloy during hot deformation. *Materials & Design, 71*, 68-77. https://doi.org/10.1016/j.matdes.2015.01.009

[23] Kim, J. H., Semiatin, S., Lee, Y. H., & Lee, C. S. (2011). A self-consistent approach for modeling the flow behavior of the alpha and beta phases in Ti-6Al-4V. *Metallurgical and Materials Transactions A, 42*(7), 1805-1814. https://doi.org/10.1007/s11661-010-0567-x

[24] Mesarovic, S. D. (1995). Dynamic strain aging and plastic instabilities. *Journal of the Mechanics and Physics of Solids*, *43*(5), 671-700. https://doi.org/10.1016/0022-5096(95)00010-G

[25] Kazim, S. M., Prasad, K., & Chakraborty, P. (2024). Analysis of dynamic strain aging in titanium alloys using CPFEM. *Materials Today: Proceedings*, *108*, 21-26. https://doi.org/10.1016/j.matpr.2023.07.268

[26] Prasad, K., & Varma, V. K. (2008). Serrated flow behavior in a near alpha titanium alloy IMI 834. *Materials Science and Engineering: A*, *486*(1-2), 158-166. https://doi.org/10.1016/j.msea.2007.09.020

[27] Prasad, Y., Rao, K., & Sasidhar, S. (2015). *Hot working guide: a compendium of processing maps*, ASM International.

[28] Bodunrin, M. O., Chown, L. H., van der Merwe, J. W., Alaneme, K. K. (2019). Hot working of Ti-6Al-4V with a complex initial microstructure. *International Journal of Material Forming*, *12*(5), 857-874. https://doi.org/10.1007/s12289-018-1457-9

[29] Seshacharyulu, T., Medeiros, S. C., Frazier, W. G., & Prasad Y. V. R. K. (2002). Microstructural mechanisms

during hot working of commercial grade Ti–6Al–4V with lamellar starting structure. *Materials Science and Engineering: A*, *325*(1-2), 112-125. https://doi.org/10.1016/S0921-5093(01)01448-4

[30] Sen, I., Kottada, R. S., & Ramamurty, U. (2010). High temperature deformation processing maps for boron modified Ti–6Al–4V alloys. *Materials Science and Engineering: A*, *527*(23), 6157-6165. https://doi.org/10.1016/j.msea.2010.06.044

[31] Zhang, J., Li, H., & Zhan, M. (2020). Review on globularization of titanium alloy with lamellar colony, *Manufacturing Review*, *7*, 18-32. https://doi.org/10.1051/mfreview/2020015

[32] Chong, Y., Bhattacharjee, T., Gholizadeh, R., Yi, J., Tsuji, N. (2019). Investigation on the hot deformation behaviors and globularization mechanisms of lamellar Ti–6Al–4V alloy within a wide range of deformation temperatures. *Materialia*, *8*, 100480. https://doi.org/10.1016/j.mtla.2019.100480